

Universal nonmonotonic structure in the saturation curves of magneto-optical-trap-loaded Na⁺ ions stored in an ion-neutral hybrid trap: Prediction and observation

R. Blümel,¹ J. E. Wells,² D. S. Goodman,^{2,3} J. M. Kwolek,² and W. W. Smith²

¹*Department of Physics, Wesleyan University, Middletown, Connecticut 06459, USA*

²*Department of Physics, University of Connecticut, Storrs, Connecticut 06269, USA*

³*Department of Sciences, Wentworth Institute of Technology, Boston, Massachusetts 02115, USA*

(Received 8 July 2015; revised manuscript received 6 October 2015; published 2 December 2015)

We predict that the maximal, steady-state ion capacity $N_s(\lambda)$ of radio-frequency (rf) traps, loaded at a rate of λ particles per rf cycle, shows universal, nonlinear, nonmonotonic behavior as a function of loading rate λ . The shape of $N_s(\lambda)$, characterized by four dynamical regimes, is universal; i.e., it is predicted to manifest itself in *all types* of rf traps independent of the details of their construction and independent of particle species loaded. For $\lambda \ll 1$ (region I), as expected, $N_s(\lambda)$ increases monotonically with λ . However, contrary to intuition, at intermediate $\lambda \sim 1$ (region II), $N_s(\lambda)$ reaches a maximum, followed by a local minimum of $N_s(\lambda)$ (region III). For $\lambda \gg 1$ (region IV), $N_s(\lambda)$ again rises monotonically. In region IV, numerical simulations, analytical calculations, and experiments show $N_s(\lambda) \sim \lambda^{2/3}$. We confirm our predictions both experimentally with magneto-optical-trap-loaded Na⁺ ions stored in a hybrid ion-neutral trap and numerically with the help of detailed *ab initio* molecular-dynamics simulations.

DOI: [10.1103/PhysRevA.92.063402](https://doi.org/10.1103/PhysRevA.92.063402)

PACS number(s): 37.10.Ty, 52.27.Jt, 52.50.Qt

I. INTRODUCTION

Radio-frequency (rf) traps [1,2] are important devices in widespread use for the long-term storage of charged particles. These traps come in a multitude of shapes and sizes [1–6] and their applications range from high-resolution spectroscopy [7] to atomic clocks [8] and quantum computers [9]. They have also been used in nonlinear dynamics for the investigation of nonlinear phenomena ranging from crystallization [10–13] to the investigation of strange attractors [14]. A fundamental problem of great theoretical and practical interest is the maximal ion capacity $N_s(\lambda)$ of rf traps loaded at a constant rate of λ particles per rf cycle. While the absolute value of N_s depends on the trap's physical size and the details of its construction, the qualitative dependence of $N_s(\lambda)$ on λ does not. In fact, we found that the shape of $N_s(\lambda)$ is universal, i.e., it is the same for any kind of rf trap, and shows four clearly defined dynamical regimes, which we label regions I to IV. In this paper, based on physical arguments and detailed *ab initio* molecular-dynamics simulations, we predict the qualitative shape of the universal curve $N_s(\lambda)$ and experimentally verify our predictions with the help of a magneto-optical-trap-loaded (MOT-loaded) ion-neutral trap [15]. While knowledge of the steady-state ion capacity N_s of rf traps in general is in itself an important fundamental problem, the results are also of practical interest in atomic physics. Collision-rate experiments [15–20], e.g., use the steady-state ion capacity to measure the total collision rate, because it ensures constant density, size, and temperature conditions during the measurement. This is particularly helpful when working with optically dark, closed-shell ions such as Rb⁺ and Na⁺.

Our paper is organized as follows. In Sec. II we present the basic dynamical equations for the three-dimensional (3D) Paul trap and the linear Paul trap used in our molecular-dynamics simulations together with the methodology according to which our simulations are performed. In this section we also present the theoretical evidence for the four nonlinear loading regimes encountered in these two trap types. In Sec. III we present

our experimental evidence that confirms the prediction of the four different dynamical regimes. In particular, in the case of the linear Paul trap, we confirm the presence of the dip characterizing the dynamical region III. In Sec. IV we discuss our results. We summarize and conclude our paper in Sec. V. We also provide an Appendix in which we derive the differential equation whose stationary solution yields the fundamental scaling relation $N_s(\lambda) \sim \lambda^{2/3}$ in region IV.

II. THEORY

Initially, we discovered the nonlinear, nonmonotonic structure of $N_s(\lambda)$ in molecular-dynamics loading simulations of a three-dimensional (3D) Paul trap. We denote by r_0 and z_0 the distances of the ring electrode and the end-cap electrodes from the trap's center, respectively; by U_0 and V_0 the amplitudes of the dc and ac voltages applied to the trap, respectively; by Γ the damping constant (generated, e.g., by laser cooling [12]); and by ω the (angular) frequency of the trap's ac voltage. The (dimensionless) equations of motion of N particles in the trap [$\vec{r} = (x, y, z)$] are [21,22]

$$\ddot{\vec{r}}_i + \gamma \dot{\vec{r}}_i + [a - 2q \sin(2t)] \begin{pmatrix} x_i \\ y_i \\ -2z_i \end{pmatrix} = \sum_{\substack{j=1 \\ j \neq i}}^N \frac{\vec{r}_i - \vec{r}_j}{|\vec{r}_i - \vec{r}_j|^3}, \quad (1)$$

where $i = 1, \dots, N$ labels the trapped particles;

$$q = \frac{4QV_0}{m\omega^2(r_0^2 + 2z_0^2)}, \quad a = \left(\frac{2U_0}{V_0}\right)q, \quad (2)$$

are the two control parameters of the Paul trap [1,12,13]; time is measured in units of

$$\tau_0 = \frac{2}{\omega}; \quad (3)$$

and distances are measured in units of

$$l_0 = (Q^2/\pi\epsilon_0 m\omega^2)^{1/3}, \quad (4)$$

where Q is the charge and m is the mass of each of the trapped particles, ϵ_0 is the permittivity of the vacuum, and

$$\gamma = \tau_0 \Gamma = \frac{2\Gamma}{\omega} \quad (5)$$

is the dimensionless damping constant. We use dimensionless quantities in this section because only this way is it possible to see that the equations of motion of particles in the Paul trap do not depend on the six physical parameters r_0 , z_0 , Γ , ω , Q , and m separately, but only on the three scaled, dimensionless parameters a , q , and γ . Therefore, instead of the need to explore a six-dimensional parameter space, which is practically impossible, we only need to explore a three-dimensional parameter space. This grows to four dimensions, if we include the loading rate λ .

In our simulations particles are created, one at a time, at times t_k , $k = 1, 2, \dots$, either with zero initial velocity (a good approximation for MOT-loaded ions [23]) or with a thermal velocity distribution as discussed below. Assuming that the creation times are uncorrelated, the time intervals $\Delta t_k = t_{k+1} - t_k$ are Poissonian distributed with probability distribution $P(\Delta t) = \lambda \exp(-\lambda \Delta t)$. Concerning their spatial distribution, we assume that the particles are created at random positions with uniform distribution within an ellipsoidal volume with semimajor axes L_x, L_y, L_z , centered at the origin of the trap. This includes the case of a spherical loading zone of radius R , in which case we have $R = L_x = L_y = L_z$. In the time interval between any two creation events, i.e., for $t_k < t < t_{k+1}$, the particles in the trap are governed by the equations of motion (1). When arriving at t_{k+1} , and before creating the next particle, we check whether one or more particles have left the trap by crossing an absorbing boundary. The existence of an absorbing boundary is a fundamental property of all rf traps, which determines and limits the storage capacity of any given trap. This boundary may be due to any number of unavoidable physical causes, such as the trap's electrodes or instabilities induced by higher-order rf multipoles [5]. Since all traps are constructed differently, and to show that our predicted effect is robust with respect to various geometries of absorbing boundaries, we used spherical boundaries of radius R_{sph} ; boxes with side lengths $2x_{\text{box}}, 2y_{\text{box}}, 2z_{\text{box}}$; and cylinders with radius R_{cyl} in the x - y plane and length $2z_{\text{cyl}} = \{[q^2/(4B)] - 1/2\}^{1/2}$ in z direction to cover a wide variety of possible boundary geometries. Following instantaneous deletion of all particles that exceed the confines of the absorbing boundary, the next particle is loaded at $t = t_{k+1}$. This procedure is followed for all t_k until a prespecified maximal simulation time is reached.

The result of a typical trap loading simulation for a spherical loading zone with $R = 3$ is shown in Fig. 1. The red (gray) fluctuating line in Fig. 1 shows the time evolution of the particle number $N(t)$ in the trap for $\lambda = 1$ as a function of t (in rf cycles) for $q = 0.2$, $a = 0.02$, and $R_{\text{sph}} = 15$. A near linear rise of $N(t)$ is followed by a sharp bend into a steady state in which $N(t)$ fluctuates around $N_s = \langle N(t) \rangle_t$, the time average of $N(t)$ in the steady state.

For many applications (see, e.g., Refs. [15,19]) it is necessary to know $N_s(\lambda)$ for a given rf trap. Figure 2 shows $N_s(\lambda)$ as a function of loading rate λ for the same Paul trap control parameters used to generate Fig. 1. The resulting curve in Fig. 2 clearly shows four distinct regimes, labeled

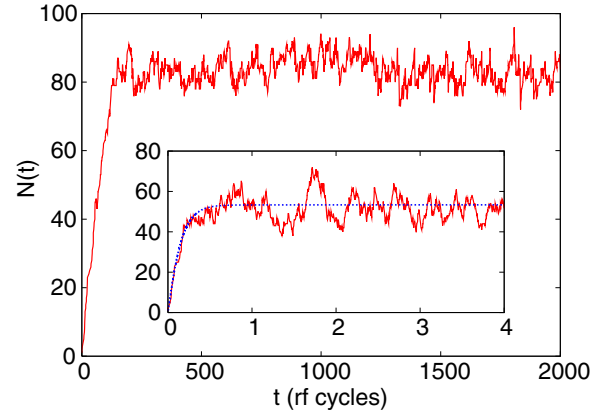


FIG. 1. (Color online) Number of particles $N(t)$ in a 3D Paul trap as a function of t (in rf cycles), loaded with loading rate $\lambda = 1$ particle / rf cycle inside of a spherical volume of radius $R = 3$ centered at the origin of the trap. Particles are absorbed at a critical distance $R_c = 15$. Trap control parameters are $\gamma = 0$, $q = 0.2$, $a = 0.02$. Inset: Test of the loading equation (6) for a loading rate $\lambda = 300$ particles / rf cycle. Red (gray) solid line: Number of particles $N(t)$ obtained via numerical simulation of the loading process. Blue (gray) dotted line: Prediction according to (8).

I to IV. Region IV is the most straightforward to understand physically; therefore, we discuss it first. In region IV, the loading rate is so large that a large space-charge density develops in the loading region. The resulting large electric field accelerates the loaded particles outward toward the absorbing boundary where the particles are lost from the trap. Since in this case the forces due to the space charge completely overwhelm the forces due to the trap fields, the particles' dynamics are accurately described as a Coulomb explosion [24]. Denoting the number of particles inside of the loading zone by $\tilde{N}(t)$ [in contrast to $N(t)$, which refers to the total number of particles

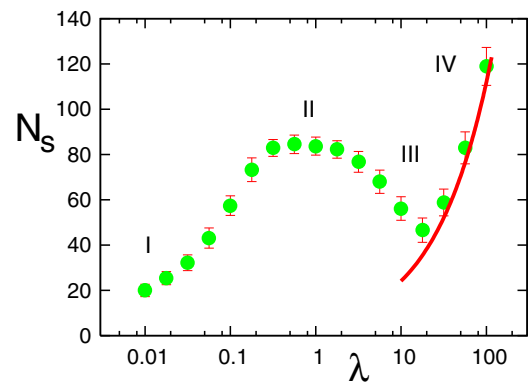


FIG. 2. (Color online) Nonmonotonic loading curve $N_s(\lambda)$ for a 3D Paul trap with $\gamma = 0$, $q = 0.2$, $a = 0.02$, $R = 3$, and $R_{\text{sph}} = 15$. Solid green (gray) dots: Results of 3D molecular dynamics loading simulations. The red (gray) bars indicate the amplitudes of the $N(t)$ fluctuations in the saturated state. For the first two dots the $N(t)$ fluctuations are smaller than the plot symbols. The four distinct regions of the loading curve are labeled I to IV. The red (gray) solid line is the curve $N_s(\lambda) = 5.2 \times \lambda^{2/3}$, which confirms the $\sim \lambda^{2/3}$ behavior of 3D Paul traps in region IV.

in the trap], the temporal evolution of the number of particles, $\tilde{N}(t)$, inside of the loading zone is governed by the differential equation (see the Appendix)

$$\frac{d\tilde{N}(t)}{dt} = \tilde{\lambda} - \left(\frac{\tilde{N}(t)}{\tilde{R}}\right)^{3/2}, \quad (6)$$

where $\tilde{R} = [16/(9\pi)]^{2/3}R \approx R$ is the effective radius of the loading volume and $\tilde{\lambda}$ is the number of particles loaded per unit of dimensionless time. According to (A1), $\tilde{\lambda}$ is related to λ , the number of particles loaded per rf cycle by $\tilde{\lambda} = \lambda/\pi$. In the stationary state, we have $d\tilde{N}(t)/dt = 0$. Therefore, we obtain from (6)

$$\tilde{N}_s(\lambda) = \tilde{R} \tilde{\lambda}^{2/3} = \left(\frac{16}{9\pi^2}\right)^{2/3} R \lambda^{2/3}. \quad (7)$$

Because of continuity, the steady-state number of particles in the trap, $N_s(\lambda)$, is proportional to the number of particles in the loading region, $\tilde{N}_s(\lambda)$. Therefore, the $\lambda^{2/3}$ dependence of $\tilde{N}_s(\lambda)$ is reflected in Fig. 2 (solid red [gray] line). Because there are more particles in the trap than there are in the loading zone, the prefactor 5.2 of $\lambda^{2/3}$, stated in the caption of Fig. 2, is larger than the prefactor $(16/\pi^2\sqrt{3})^{2/3} \approx 1$ of $\lambda^{2/3}$, computed from (7) with $R = 3$.

The solution of (6) can be stated implicitly in closed form:

$$t = -\frac{2\tilde{R}}{3\tilde{\lambda}^{1/3}} \left\{ \ln(\alpha - \tilde{N}^{1/2}) - \frac{1}{2} \ln(\tilde{N} + \alpha\tilde{N}^{1/2} + \alpha^2) + \sqrt{3} \arctan\left(\frac{2\tilde{N}^{1/2} + \alpha}{\alpha\sqrt{3}}\right) - \sqrt{3} \arctan\left(\frac{1}{\sqrt{3}}\right) \right\}, \quad (8)$$

where $\alpha = \tilde{R}^{1/2}\tilde{\lambda}^{1/3}$. That (8) is indeed a solution of (6) may be checked immediately by differentiating (8) with respect to t . Since the trap potentials are not important in region IV, the results (6)–(8) apply universally to *all* rf traps, for instance 3D or linear Paul traps.

In order to test (8), we chose $\tilde{R} = 3$ and a large loading rate of $\lambda = 300$ particles / rf cycle to be sure that we are in region IV. The result of the corresponding molecular dynamics simulation of $N(t)$ is shown as the solid, fluctuating red (gray) line in the inset of Fig. 1. The blue (gray) dotted line in the inset of Fig. 1 is the prediction according to (8). Both agree perfectly within the expected fluctuations of $N(t)$, which are due to the Poissonian loading process.

While for large λ the trap potentials are not important, they become progressively more important when λ is lowered. In this case, for sufficiently low λ , particles created close to the edge of the loading zone no longer have enough energy to overcome the trap potentials and are reflected back into the interior of the trap. When back-reflection occurs, fewer particles escape and $N_s(\lambda)$ increases for decreasing λ up to a maximum in region II, effectively creating a dip in region III (see Fig. 2). However, the reflected particles will not stay in the trap forever. Due to rf heating [12,21], and given enough time (small loading rates), these particles will heat out of the trap, eventually lowering the number $N_s(\lambda)$ of stationary-state particles in the trap below the bottom of the dip in region III (see Fig. 2), thus explaining both the formation of the maximum in $N_s(\lambda)$ (region II in Fig. 2) and the eventual decline of $N_s(\lambda)$ in the direction of ever diminishing loading rates

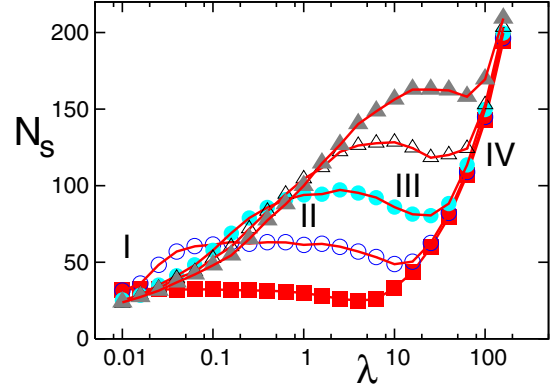


FIG. 3. (Color online) 3D Paul trap capacities $N_s(\lambda)$ for various trap control parameters q and $\gamma = 0$. Solid red (gray) squares: $q = 0.1$; open blue (gray) circles: $q = 0.15$; solid cyan (gray) circles: $q = 0.2$; open black triangles: $q = 0.25$; solid gray triangles: $q = 0.3$. The trap parameter a associated with each of the five q values is $a = q^2/2$. The four dynamical regimes are labeled I to IV. The solid red (gray) lines connecting the data points are drawn to guide the eye. All five curves asymptote to $N_s(\lambda) \sim \lambda^{2/3}$ for large λ .

(region I in Fig. 2). Since rf heating is a universal feature of all rf charged-particle traps, we predict that the qualitative shape of $N_s(\lambda)$ is universal for all rf traps.

To strengthen the claim of universality of the nonmonotonic curve shown in Fig. 2, we show in Fig. 3 the saturated number of particles $N_s(\lambda)$ as a function of loading rate λ for several values of q with $a = q^2/2$, $L_x = L_y = 3$, $L_z = 6$, and $x_{\text{box}} = y_{\text{box}} = z_{\text{box}} = 15$. All five curves in Fig. 3 clearly show all four dynamical regimes, again labeled I to IV. This shows that the nonmonotonic behavior is robust with respect to (a) a change in q , (b) a change in the geometry of the loading zone (spherical in Fig. 2; ellipsoidal in Fig. 3), and (c) a change in the geometry of the absorbing boundary (spherical in Fig. 2; cubic in Fig. 3). This applies in particular to region IV, in which all five curves in Fig. 3 are seen to converge to the same $\sim \lambda^{2/3}$ asymptote. The independence of a and q in region IV is explained by (6), which is independent of the trap potentials and therefore independent of the trap parameters a and q . Figure 3 also shows that the dip becomes shallower with both increasing and decreasing q and shifts to the right with increasing q . In addition, we see that region II becomes more extended with decreasing q . At present we do not have a theoretical explanation for these observed effects.

To check the universality of the nonmonotonic behavior, we also simulated a linear Paul trap [25] whose equations of motion, in the notation and units of (1), are given by

$$\begin{pmatrix} \ddot{x}_i + [a - 2q \sin(2t)]x_i - Bx_i \\ \ddot{y}_i - [a - 2q \sin(2t)]y_i - By_i \\ \ddot{z}_i + 2Bz_i \end{pmatrix} = \sum_{\substack{j=1 \\ j \neq i}}^{N_k} \frac{\vec{r}_i - \vec{r}_j}{|\vec{r}_i - \vec{r}_j|^3}, \quad (9)$$

where B is a positive constant. We simulate the loading process of the linear Paul trap in analogy to the 3D Paul trap as discussed above with a loading region of radius $R = 3$, located at the geometric center of the linear trap and a cylindrical absorbing boundary with $R_{\text{cyl}} = 15$. This time, however, we use the equations of motion (9) between creation times.

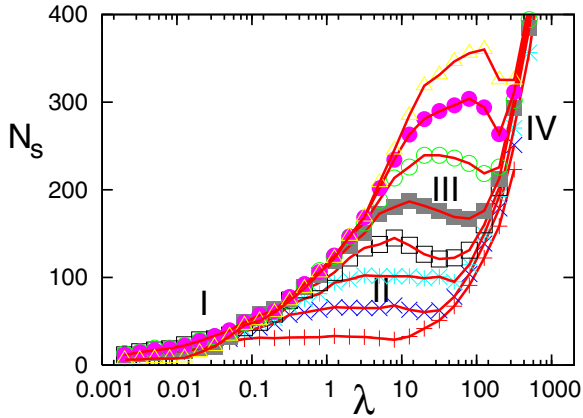


FIG. 4. (Color online) Saturation curves $N_s(\lambda)$, for a linear Paul trap. Pluses (red [gray]): $q = 0.35$; crosses (blue [gray]): $q = 0.40$; diamonds (cyan [gray]): $q = 0.45$; open squares (black): $q = 0.50$; solid squares (gray): $q = 0.55$; open circles (green [gray]): $q = 0.60$; solid circles (magenta [gray]): $q = 0.65$; open triangles (brown [gray]): $q = 0.70$. The solid lines (red [gray]) connecting the data points are drawn to guide the eye. All eight curves asymptote to $N_s(\lambda) \sim \lambda^{2/3}$ for large λ . The labels I to IV refer to the four different dynamical regimes.

Figure 4 shows the resulting $N_s(\lambda)$ for eight different q values with $a = 0$ and $B = 0.042$. We clearly see the four different regions of $N_s(\lambda)$, observed previously in the case of the 3D Paul trap. This provides corroborating evidence for the universal nature of the shape of $N_s(\lambda)$ for all types of rf traps.

III. EXPERIMENT

The ultimate test of our theoretical predictions is an experiment. For this purpose we used a MOT-loaded ion-neutral hybrid trap [15]. Figure 5 shows the results of our experiments. All four predicted dynamical regimes are present and the shape of the experimental $N_s(\lambda)$ curve is seen to be qualitatively the same as predicted by the model simulations and our

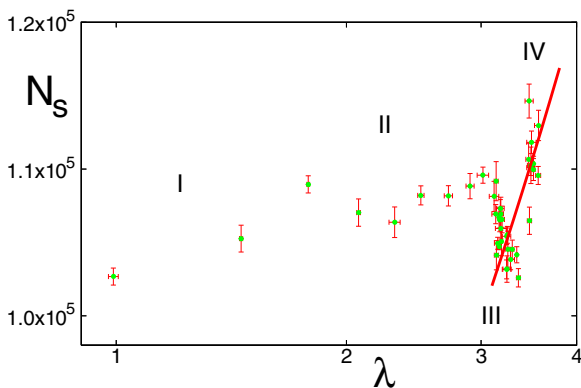


FIG. 5. (Color online) Experimental saturation curve for the hybrid trap [15], operated with $q = 0.26$. All four predicted dynamical regimes are present. The solid line (red [gray]) is the curve $N_s = 48000\lambda^{2/3}$. The error bars represent the statistical errors associated with multiple data runs. The zero point of the horizontal scale is suppressed.

qualitative analysis of the physical mechanisms that determine the steady-state populations in rf traps. From the experimental data we obtain $\epsilon = 0.745 \pm 0.098$ for the exponent ϵ in $N_s(\lambda) \sim \lambda^\epsilon$, which is consistent with the predicted value $\epsilon = 2/3$ in region IV (solid line in Fig. 5). We note that, corroborating the universality claim, the qualitative shape of the nonlinear, nonmonotonic behavior of $N_s(\lambda)$ was observed in all of our simulations and experiments, independent of rf amplitudes, rf frequencies, and MOT sizes. With a depth of about 5%, the dip in Fig. 5 is small. However, notice that the experimental q of $q = 0.26$ is small; this observation is consistent with Fig. 4, which shows that the depth of the dip decreases with decreasing q .

IV. DISCUSSION

To strengthen the universality claim and to emphasize the robustness of our predictions, we performed numerous additional simulations that all confirmed that the qualitative shape of the saturation curve, characterized by its four dynamical regimes, is insensitive to both the type of traps used and their particular loading mechanisms. In particular, we performed additional simulations with (a) various shapes of the loading ellipse with aspect ratios of $L_x : L_y : L_z$ up to 1:1:4, (b) replacing the Poissonian distribution of loading times with a uniform distribution, (c) replacing the uniform spatial distribution with a Gaussian distribution, (d) various geometries of the absorbing boundary and boundary locations, and (e) increasing the number of trapped particles to up to 1000 by changing the diameter of the absorbing boundary. All five numerical tests confirmed the qualitative shape of $N_s(\lambda)$ as shown in Figs. 2–5. In addition, we performed the following two checks concerning ion cooling and the effect of temperature.

In many ion-trap experiments, strong laser cooling is continuously switched on, even during the loading stage (see, e.g., Ref. [12]). Therefore, to test the influence of cooling during trap loading, we ran additional 3D Paul-trap loading simulations with strong damping switched on, so strong in fact, that it would crystallize the ions [10–12,25] if we were not constantly loading. This corresponds to γ values between 5×10^{-4} and 10^{-3} . As a result we find that we still have all four dynamical regimes, in particular the dip. Moreover, the $N_s(\lambda)$ curves in the two cases (with and without damping, respectively) are nearly identical, differing from each other only within the natural fluctuations of N_s due to the Poissonian loading process. In some of our more recent simulations, just to push the envelope, we increased the damping to five times the one needed for crystallization ($\gamma = 5 \times 10^{-3}$). It still did not have any effect on the qualitative shape of the loading curves. Thus, we conclude that the presence of laser cooling that can realistically be achieved experimentally has no effect on our predicted phenomena. We also mention that a large laser cooling power does not necessarily result in a large γ , since γ represents the balance between laser cooling and the substantial amount of heating caused by the loading process.

In our experiments we load from a cold MOT and the assumption of zero kinetic energy at the instance of charged-particle creation is justified. However, in case the trap is loaded by ionizing the rest gas or via a thermal neutral beam, the particles may be created with substantial initial kinetic energy.

To test the effect of initial kinetic energy on our predictions, we performed additional loading simulations, imparting a random velocity on each particle at the instant of its creation whose energy equivalent was up to 20% of the trap depth. In our experiments this would be equivalent to about room temperature. Even in this case we are still able to observe all four dynamical regions. The explanation is that in steady state there is an equilibrium between particles created and particles leaving the trap. Those that leave already have kinetic energies of the order of the trap's depth, which they are able to impart, via Coulomb collisions, to newly created particles. Therefore, the fact that particles are created with a kinetic energy less than the trap's depth is only a minor perturbation on the energetic particle dynamics that is already going on inside of the trap.

In our simulations we found that the dip in region III is more pronounced if the absorbing boundaries are further from the edges of the loading zone. This observation explains why the dip is more pronounced in Fig. 2 compared with the dips in Fig. 3. In Fig. 3 we used an elliptical loading zone with $L_z = 6$ compared with the spherical loading zone in Fig. 2 with $R = 3$. Therefore, in the z direction, it is easier for the particles in Fig. 3 to bridge the gap to the absorbing boundary, because many of them are already created closer to the absorbing boundary. The shorter distance to cover results in a shallower dip.

V. SUMMARY AND CONCLUSIONS

In this paper we report the discovery of the nonmonotonic shape of the saturated ion number $N_s(\lambda)$ of rf traps as a function of loading rate λ and present evidence for its universality. Four dynamical regions are predicted. In region I, $N_s(\lambda)$ increases monotonically with λ , reaching a maximum (region II) at intermediate loading rates λ , followed by a valley (region III), and an ultimate $\sim \lambda^{2/3}$ increase of $N_s(\lambda)$ for very large loading rates. We argue that the four regions are expected on the basis of physical reasons and are caused by the interplay between trap potentials, space-charge effects, and rf heating. The validity of our predictions, in particular their universality, is corroborated with the help of *ab initio* molecular-dynamics simulations of a 3D Paul trap and a linear Paul trap, which both show the predicted qualitative shape of $N_s(\lambda)$. The theoretical predictions are confirmed experimentally with the help of Na^+ ions in a MOT-loaded linear Paul trap.

Apart from our research group [15], several other groups [16–20] have the necessary experimental facilities to test our predictions in the case of MOT-loaded traps, and since, as we showed, the predicted phenomenon is robust with respect to rf trap types, loading mechanisms, and temperature effects, we hope that other research groups may soon test and confirm our predictions.

ACKNOWLEDGMENT

Financial support by NSF Grant No. PHY-1307874 is gratefully acknowledged.

APPENDIX: REGION IV DIFFERENTIAL EQUATION

In this Appendix we present a simple, explicitly solvable, analytical model that reproduces the $\lambda^{2/3}$ scaling of N_s in

region IV, the fast-loading regime. While in Sec. II we used dimensionless quantities to bring out the scaling properties of the Paul-trap equations, it is more convenient in this Appendix to derive our equations using SI units. In these units, we denote time (measured in seconds) by τ , the loading rate (measured in particles per second) by Λ , and the radius of the loading zone (measured in meters) by \hat{R} . However, in order to make contact with the formulas in Sec. II, it is convenient to define λ , as we did in Sec. II, as the number of particles loaded per rf cycle, and by

$$\tilde{\lambda} = \tau_0 \Lambda = 2\Lambda/\omega = \lambda/\pi \quad (\text{A1})$$

the dimensionless loading rate per unit of dimensionless time. The unit of time, τ_0 , in (A1) is defined in (3). The last equality in (A1) comes about since in dimensionless time an rf cycle has a length of π [see (1)].

We are now ready to start our derivation of Eq. (6) in Sec. II, which holds in region IV. As discussed in Sec. II, in this region we may neglect the trap potential altogether. We assume that the trapped particles are created at random locations inside of a sphere of radius R with uniform probability distribution and loading rate λ . If there are \tilde{N} particles present inside the sphere of radius \hat{R} , the charge density, approximated as a continuous distribution, is

$$\rho = \frac{3\tilde{N}Q}{4\pi\hat{R}^3}, \quad (\text{A2})$$

where Q is the charge of each trapped particle. Using Gauss's law, the radial electric field, pointing outward, a distance r away from the center of the sphere, is

$$E = \frac{\rho r}{3\epsilon_0}. \quad (\text{A3})$$

Therefore, the radial, outward-directed force experienced by an ion a distance r away from the loading sphere is

$$F = \left(\frac{\rho Q r}{3\epsilon_0} \right) = \left(\frac{\tilde{N} Q^2}{4\pi\epsilon_0 \hat{R}^3} \right) r. \quad (\text{A4})$$

This equation shows that the force experienced by a single trapped particle is like the harmonic force of an inverted oscillator. Therefore, the equation of motion of the ion is

$$m\ddot{r} = F \Rightarrow \ddot{r} = \tilde{N}\Omega^2 r, \quad (\text{A5})$$

where m is its mass and

$$\Omega = \left(\frac{Q^2}{4\pi\epsilon_0 m \hat{R}^3} \right)^{1/2}. \quad (\text{A6})$$

The general solution of (A5) is

$$r(\tau) = A \exp(\sqrt{\tilde{N}\Omega^2}\tau) + B \exp(-\sqrt{\tilde{N}\Omega^2}\tau), \quad (\text{A7})$$

where A and B are constants. If we assume that at $\tau = 0$ the particle is created a distance s away from the center of the loading sphere, (A7) may be written as

$$r(\tau) = s \cosh(\sqrt{\tilde{N}\Omega^2}\tau), \quad (\text{A8})$$

and the velocity of the particle is

$$\dot{r}(\tau) = s\sqrt{\tilde{N}\Omega^2} \sinh(\sqrt{\tilde{N}\Omega^2}\tau). \quad (\text{A9})$$

Define T_0 as the time it takes the particle to reach the rim of the loading sphere at radius \hat{R} if the ion starts at radius s with zero velocity. Then

$$\hat{R} = s \cosh(\sqrt{\tilde{N}\Omega T_0}) \quad (\text{A10})$$

$$\Rightarrow \cosh(\sqrt{\tilde{N}\Omega T_0}) = \frac{\hat{R}}{s}. \quad (\text{A11})$$

When it arrives at \hat{R} , the velocity of the ion is

$$v_0 = s\sqrt{\tilde{N}\Omega} \sinh(\sqrt{\tilde{N}\Omega T_0}). \quad (\text{A12})$$

Use (A11), together with $\cosh^2(x) - \sinh^2(x) = 1$, to write (A12) in the form

$$v_0 = \sqrt{\tilde{N}\Omega} \sqrt{\hat{R}^2 - s^2}. \quad (\text{A13})$$

Next, we compute the average velocity \bar{v}_0 with which a randomly created particle arrives at \hat{R} . Denoting by \mathcal{V} the volume of the loading sphere, $\mathcal{V} = 4\pi \hat{R}^3/3$, and using the fact that we assume a uniform probability distribution of particle creation positions within the sphere, we obtain

$$\begin{aligned} \bar{v}_0 &= \frac{\sqrt{\tilde{N}\Omega}}{\mathcal{V}} \int_{\mathcal{V}} \sqrt{\hat{R}^2 - s^2} dV \\ &= \frac{3\sqrt{\tilde{N}\Omega}}{\hat{R}^3} \int_0^{\hat{R}} s^2 \sqrt{\hat{R}^2 - s^2} ds = \frac{3}{16} \pi \hat{R} \Omega \sqrt{\tilde{N}}. \end{aligned} \quad (\text{A14})$$

Since the average ion arrives at \hat{R} with an average velocity \bar{v}_0 , directed radially outward, the average number dN_l of particles lost from the loading sphere in time $d\tau$ is the number of particles in a shell of radius \hat{R} and width $\bar{v}_0 d\tau$. Explicitly,

$$dN_l = \frac{\rho}{Q} 4\pi \hat{R}^2 \bar{v}_0 d\tau = \left(\frac{9\pi}{16}\right) \tilde{N}^{3/2} \Omega d\tau. \quad (\text{A15})$$

The number of particles gained due to loading with rate Λ is

$$dN_g = \Lambda d\tau. \quad (\text{A16})$$

Therefore the total change $d\tilde{N}$ in the number of particles present in the loading sphere is

$$d\tilde{N} = dN_g - dN_l = \Lambda d\tau - C \tilde{N}^{3/2} d\tau, \quad (\text{A17})$$

where

$$C = \frac{9\pi}{16} \left(\frac{Q^2}{4\pi \epsilon_0 m \hat{R}^3} \right)^{1/2}. \quad (\text{A18})$$

Dividing (A17) by $d\tau$, we obtain a first-order differential equation for the number of particles \tilde{N} inside the loading sphere:

$$\frac{d\tilde{N}}{d\tau} = \Lambda - C \tilde{N}^{3/2}. \quad (\text{A19})$$

To transform this equation into its dimensionless form, we use the unit of time, τ_0 , and the unit of length, l_0 , defined in (3) and (4), respectively, which relates τ , Λ , and \hat{R} in SI units to their dimensionless counterparts, t , λ , and R , respectively, according to [see also (A1)]

$$\tau = t\tau_0, \quad \Lambda = \tilde{\lambda}/\tau_0, \quad \hat{R} = Rl_0. \quad (\text{A20})$$

Using (A20) in (A19) and defining

$$\tilde{R} = \left(\frac{16}{9\pi} \right)^{2/3} R, \quad (\text{A21})$$

we arrive at

$$\frac{d\tilde{N}}{dt} = \tilde{\lambda} - \left(\frac{\tilde{N}(t)}{\tilde{R}} \right)^{3/2}, \quad (\text{A22})$$

which is identical with (6) of Sec. II.

-
- [1] W. Paul, *Rev. Mod. Phys.* **62**, 531 (1990).
[2] P. K. Ghosh, *Ion Traps* (Clarendon Press, Oxford, 1995).
[3] H. Dehmelt and N. Yu, *Proc. Natl. Acad. Sci. USA* **94**, 10031 (1997).
[4] C. Champenois, M. Knoop, M. Herbane, M. Houssin, T. Kaing, M. Vedel, and F. Vedel, *Eur. Phys. J. D* **15**, 105 (2001).
[5] R. Alheit, Th. Gudjons, S. Kleineidam, and G. Werth, *Rapid Commun. Mass Spectrom.* **10**, 583 (1996).
[6] C. A. Schrama, E. Peik, W. W. Smith, and H. Walther, *Opt. Commun.* **101**, 32 (1993).
[7] J. C. Bergquist, W. M. Itano, and D. J. Wineland, *Phys. Rev. A* **36**, 428 (1987).
[8] J. C. Bergquist, S. R. Jefferts, and D. J. Wineland, *Phys. Today* **54**, 37 (2001).
[9] J. I. Cirac and P. Zoller, *Phys. Rev. Lett.* **74**, 4091 (1995).
[10] F. Diedrich, E. Peik, J. M. Chen, W. Quint, and H. Walther, *Phys. Rev. Lett.* **59**, 2931 (1987).
[11] D. J. Wineland, J. C. Bergquist, W. M. Itano, J. J. Bollinger, and C. H. Manney, *Phys. Rev. Lett.* **59**, 2935 (1987).
[12] R. Blümel, J. M. Chen, E. Peik, W. Quint, W. Schleich, Y. R. Shen, and H. Walther, *Nature (London)* **334**, 309 (1988).
[13] R. Blümel, C. Kappler, W. Quint, and H. Walther, *Phys. Rev. A* **40**, 808 (1989).
[14] R. G. Brewer, J. Hoffnagle, R. G. DeVoe, L. Reyna, and W. Henshaw, *Nature (London)* **344**, 305 (1990).
[15] D. S. Goodman, J. E. Wells, J. M. Kwolek, R. Blümel, F. A. Narducci, and W. W. Smith, *Phys. Rev. A* **91**, 012709 (2015).
[16] A. T. Grier, M. Cetina, F. Oručević, and V. Vuletić, *Phys. Rev. Lett.* **102**, 223201 (2009).
[17] S. T. Sullivan, W. G. Rellergert, S. Kotochigova, K. Chen, S. J. Schowaltera, and E. R. Hudson, *Phys. Chem. Chem. Phys.* **13**, 18859 (2011).
[18] K. Ravi, S. Lee, A. Sharma, G. Werth, and S. A. Rangwala, *Nat. Commun.* **3**, 1126 (2012).
[19] S. Lee, K. Ravi, and S. A. Rangwala, *Phys. Rev. A* **87**, 052701 (2013).
[20] T. Ray, S. Jyothi, N. B. Ram, and S. A. Rangwala, *Appl. Phys. B* **114**, 267 (2014).
[21] J. D. Tarnas, Y. S. Nam, and R. Blümel, *Phys. Rev. A* **88**, 041401(R) (2013).
[22] Y. S. Nam, E. B. Jones, and R. Blümel, *Phys. Rev. A* **90**, 013402 (2014).
[23] D. S. Goodman, I. Sivarajah, J. E. Wells, F. A. Narducci, and W. W. Smith, *Phys. Rev. A* **86**, 033408 (2012).
[24] Z. Vager, R. Naaman, and E. P. Kanter, *Science* **244**, 426 (1989).
[25] M. G. Raizen, J. M. Gilligan, J. C. Bergquist, W. M. Itano, and D. J. Wineland, *Phys. Rev. A* **45**, 6493 (1992).